Real-Time Sensing of Sag Geometry During GTA Welding

Y. M. Zhang
Mem. ASME

R. Kovacevic
Mem. ASME

Welding Research and Development Laboratory,
Center for Robotics and Manufacturing Systems,
University of Kentucky,
Lexington, KY

Seam tracking and weld penetration control are two fundamental issues in automated welding. Although the seam tracking technique has matured, the latter still remains a unique unsolved problem. It was found that the full penetration status during GTA welding can be determined with sufficient accuracy using the sag depression. To achieve a new full penetration sensing technique, a structured-light 3D vision system is developed to extract the sag geometry behind the pool. The laser stripe, which is the intersection of the structured-light and weldment, is thinned and then used to acquire the sag geometry. To reduce possible control delay, a small distance is selected between the pool rear and laser stripe. An adaptive dynamic search for rapid thinning of the stripe and the maximum principle of slope difference for unbiased recognition of sag border were proposed to develop an effective real-time image processing algorithm for sag geometry acquisition. Experiments have shown that the proposed sensor and image algorithm can provide reliable feedback information of sag geometry for the full penetration control system.

1 Introduction

Weld penetration is critical in generating sound joints. It is usually specified by the penetration depth or back-side bead width for the partially and fully penetrated joints, respectively. When designing practical control systems, it is often believed that the sensors should obtain their information from the weld-face so they can be mounted on and move with the torch. However, neither the penetration depth nor the back-side bead width can be directly viewed from the weld-face. Thus, sensing the weld penetration using a weld-face sensor has been an important but difficult issue. To solve this problem, a number of approaches, for example, pool oscillation, infrared sensing, ultrasound, etc., have been proposed. These approaches have been reviewed in our previous paper [1]. Recently, Xiao and Ouden reported an abrupt change in the oscillation frequency of the pool during the transition from the partial to full penetration [2, 3]. However, it is unlikely that the oscillation can provide accurate measurements of either the penetration depth or back-side bead width of the weld pool. For example, in practical welding, the desired back-side bead width could be selected from 3 to 5 mm. However, the oscillation frequency is not sensitive to the variation in the back-side bead width in this range (Fig. 13 in [2]). For ultrasonic sensing, a critical problem is the use of contact sensors. Although non-contact sensors have been tried, severe problems arise [4]. It seems that although significant progress has been made in this area, new methods are still strongly needed due to the specific limitations associated with each individual method.

The primary function of the root pass is to produce a desired full penetration status. In order to acquire quality joints, the root pass is frequently gas tungsten arc (GTA) welded. Thus, full penetration sensing in GTA welding should be one of the most important research issues in automated welding. This study will focus on this issue. In our initial study [1], the correlation between the back-side bead width and weld-face sag geometry during GTA welding was investigated. It was found that the back-side bead width can be determined with sufficient accuracy using the sag depression based on a simple linear correlation. This correlation reflects the inherent dependence of the weld pool depression of a fully penetrated pool on its back-side opening. Similar correlations have also been observed between the weld pool depression and penetration depth [5, 6].

To acquire a new sensing technique for precise penetration control, a vision system is developed. Based on the analysis of the image features, software is developed to process the acquired image in real-time. Using the provided feedback of sag parameters, a closed-loop control system has been developed to control the full penetration. To show the effectiveness of the developed sensing technology, examples of the on-line measurements and closed-loop control experiments will also be given in this paper.

2 Background

Figure 1 shows the cross section of a fully penetrated joint. Conventionally, the sag depression depth H, sag width b, and back-side bead width b_b are used to describe the cross section geometrically. It was observed that when H and b were utilized to describe b_b, no adequate relationship could be found. Thus, the average sag depression depth $h = S/b$ is defined as a new weld-face parameter (Fig. 1). Here S is the weld-face depression area of the cross section (Fig. 1).

In our initial study, experiments have been performed under a variety of welding conditions [1]. It was found that b_b can be sufficiently determined by only h [1]. Thus, the full penetration status can be monitored by sensing the sag geometry.

3 Image System

In order to measure the sag geometry, 3D vision is required. Among existing 3D vision sensing techniques (such as texture [7], shading [8], multi-cameras [9], and structured-light [10] etc.), the structured-light method is the most promising technique for our application due to its simplicity in computation and high signal-noise ratio. Consequently, the vision system shown in Fig. 2 is proposed. This system consists of a computer, frame grabber, laser, optical fibre, cylindrical lens, camera, and narrow-band optical filter. The structured-light plane is produced and projected onto the sag using a cylindrical lens. When the light plane is projected onto the sag, a laser stripe forms. The sag geometry is contained in the stripe. The image is referred to as the sag-stripe image. In order to suppress the disturbances due to the arc light and due to the radiation from the hot metal, a narrow-band filter has been employed. The main technical data of the sensing system is listed in Table 1.

Contributed by the Manufacturing Engineering Division for publication in the JOURNAL OF MANUFACTURING SCIENCE AND ENGINEERING. Manuscript received April 1995; revised Sept. 1995. Associate Technical Editor: E. Kannatey-Asibu.

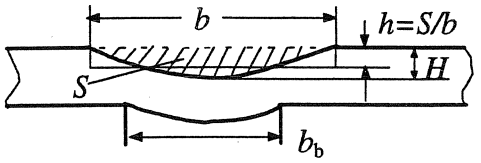

Fig. 1 Cross section of a fully penetrated joint. The average sag depression depth h is defined by the ratio between the depression area S and the sag width b. The back-side bead width b_b is used to specify the status of joint penetration.

The measurement accuracy of the sag geometry is primarily determined by the image signal-noise ratio, resolution and processing technique. The signal-noise ratio can be increased by increasing the intensity of structured-light and increasing the distance between the pool rear and laser stripe. To obtain a high signal-noise ratio, the structured-light should be a series of laser spots projected onto the sag by a scanning optical configuration [11–13]. However, for safety reasons, a too high intensity laser must not be used. In arc welding sensing, the laser power is, in general, under twenty milliwatts and the diameter of the laser spot is approximately one millimeter. The corresponding intensity is less than 100 mW/mm^2. In order to avoid a complicated scanning mechanism, a laser stripe with uniform intensity can be directly produced utilizing a more powerful laser and a cylindrical lens. For this intensity, the distance from the pool rear to laser stripe should not be too small (Fig. 3) in order to suppress the radiation from the hot metal. However, a larger distance will produce a larger delay for the weld penetration control. A trade-off between the image processing and the control delay must be considered. Experiments have shown that a satisfactory performance of image processing can be achieved using the image processing technique proposed in this paper if the distance from the pool rear to the stripe is larger than 5 mm. In this case, acceptable control performance can be obtained by a robust adaptive control algorithm [14]. Thus, the laser stripe is projected 20 mm behind the electrode. The resultant sag-stripe image is shown in Fig. 4.

The laser stripe should also illuminate the unmolten workpiece in order to determine the sag border. Since the sag width varies from a few millimeters to ten millimeters, the length of the laser stripe is selected to be about 20 mm. The width of the field of view is selected to be 25.6 mm accordingly. The resultant resolution along the width direction, i.e., the X axis on the image plane, is 0.05 mm (pixel$_x$ = 0.05 mm). The resolution along the depression direction, i.e., the Y axis on the image plane, is 0.0436 mm (pixel$_y$ = 0.0436 mm).

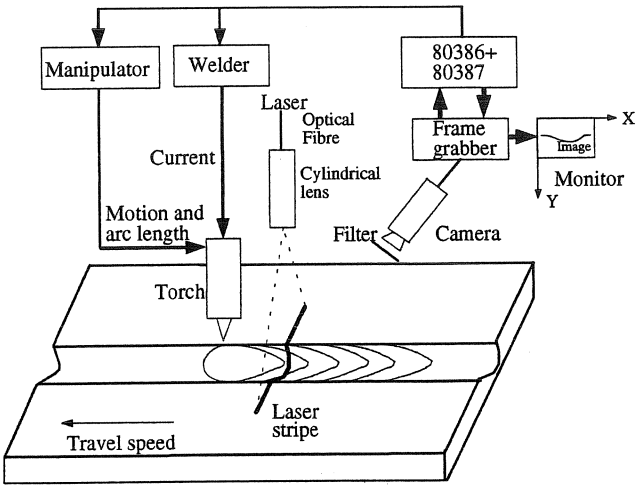

Fig. 2 Structured-light 3D image system. The laser stripe is projected onto the sag behind the weld pool rear. The deformation information of the sag is contained in the deformed stripe. The deformed stripe is acquired by the camera and then processed by the computer (80386 + 80387). The camera and lens of the laser projector are attached to and move with the torch.

Table 1 Sensor technical data

Computer	80386+80387
Frame grabber	8 bit, 512×512, 30 frames/s
Laser	Nd: YAG, 1.06 μm 0.1 - 33 W adjustable
Optical filter	wavelength: 1.0579 μm half width band: 0.0123 μm
Camera	National V-260

4 Case Analysis

Before the image is processed, a brief analysis should be made. The required speed of the image processing should be determined. To develop the processing algorithm, the image feature must also be analyzed. Then the major steps in the image processing can be designed accordingly.

A typical GTA welding speed, 2 mm per second, will be used in the control experiments [14]. In order to acquire a fine and smooth full penetration, the control variables should be frequently adjusted along the weld seam. These adjustments are made at 1 mm increments [14]. The corresponding sampling interval of the control system is 0.5 second. Within this period, both image processing and control algorithm calculation have to be performed. Thus, the real-time image processing must be performed in 0.4 second or less, leaving 0.1 second for the control algorithm.

Structured-light 3D vision sensors have been applied to preview the weld seam for the purpose of seam tracking [10, 15, 16]. However, when the sag behind the pool rear is sensed, much stronger image disturbances will be present. Also, in the case of seam tracking, the feature of the weld preparation is

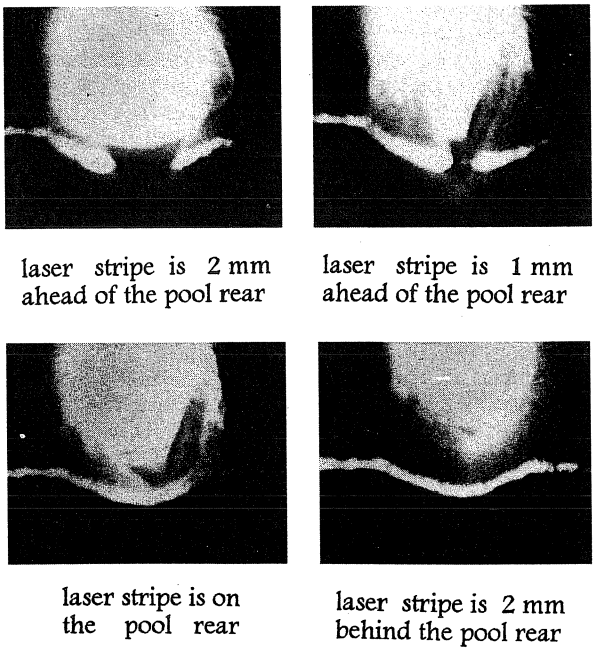

Fig. 3 Influence of stripe location on the signal-noise ratio. The images in this figure were acquired by projecting the laser stripe in the neighborhood of the pool rear. Because the distance between the weld pool and laser stripe is too small or even the stripe is on the weld pool, the laser stripe is not easy to detect. A minimum allowed distance between laser and pool rear is required.

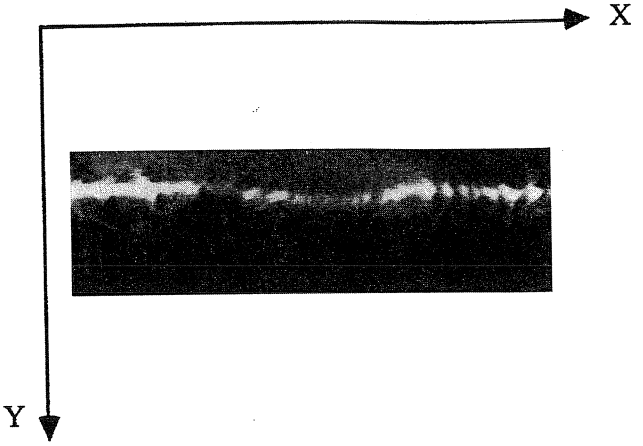

Fig. 4 Typical sag-stripe image. In this case, the distance between the laser stripe and pool rear is not less than 5 mm. The laser stripe can be clearly observed.

usually easily identifiable (Fig. 5). In GTA welding without filler, the deformation of the sag is small and, therefore, the sag border is much more difficult to identify. Thus, a more complicated arc welding sensing problem is encountered. In general, the following five steps are required to acquire the sag geometric parameters from the sag-stripe images: (1) Image filtering or noise suppression, (2) Binarization of the image, (3) Extraction of stripe skeleton, i.e., laser stripe thinning, (4) Sag border recognition, and (5) Computation of sag geometric parameters based on the medial axis and border points.

The above procedures are time-consuming. If a robust algorithm can be designed to extract the skeleton of the laser stripe accurately and rapidly, the first two steps may be skipped. The processing time will be reduced. Also, it is known that the sag border can greatly influence the final results of the calculated sag parameters. Because of the small sag depression and possible stripe skeleton extraction error, a sophisticated statistical algorithm must also be designed to improve the accuracy. In this study, two separate algorithms have been proposed for extraction of the skeleton and sag border. The resultant image processing technique can therefore be characterized by the following three steps: (1) Adaptive dynamic extraction of stripe skeleton, (2) Statistic recognition of sag border, and (3) Sag geometric parameters computation.

5 Stripe Skeleton

The stripe skeleton, referred to as the medial axis [17], contains the geometrical information about the sag. The skeleton will be acquired by thinning the stripe. An adaptive dynamic thinning algorithm will be proposed to directly extract the stripe skeleton from the gray-level image. The need for image binarization is therefore eliminated.

Assume $(k, y_0(k))$ to be the maximum grayness point across the laser stripe along the line $x = k$ (Fig. 6(a)). This point is referred to as the medial point of the laser stripe along the line $x = k$. The set of medial points $(k, y_0(k))$'s $(k = 1, \ldots, K)$ can be defined as the medial axis of the laser stripe in the interval $[x = 1, x = K]$, and the objective of the thinning operation is to obtain this medial axis.

In general, a window is selected to reduce the size of the image to be processed. The location of the laser stripe in the image may vary during welding. Although a window may be selected on-line to trace the variation in the laser stripe location, the size of the window can not be too small in order to guarantee that the laser stripe is always within the window. The thinning speed is therefore affected.

In order to solve the conflict between the computational speed and window size, a dynamic thinning procedure (DTP) is proposed based on the assumption that the laser stripe is continuous. The essence of this procedure is to begin the search for the maximum grayness point from an initial point. Because the laser stripe is usually continuous along the X direction, $y_0(k-1)$ can be used as the initial Y coordinate for finding $y_0(k)$ (Fig. 7). Also, in order to improve the robustness of the thinning operation, the maximum allowed $|y_0(k) - y_0(k-1)|$ has been limited to be 1 (pixel$_y$):

$$\begin{cases} \text{if} \quad y_0(k) = y_0(k-1), & \text{let} \quad y_0(k) = y_0(k-1) \\ \text{if} \quad y_0(k) > y_0(k-1), & \text{let} \quad y_0(k) = y_0(k-1) + 1 \\ \text{if} \quad y_0(k) < y_0(k-1), & \text{let} \quad y_0(k) = y_0(k-1) - 1 \end{cases} \tag{1}$$

It has been shown that if the assumption on the continuity of the laser stripe is true, the DTP can successfully extract the medial axis from the small dynamic search ranges (Fig. 7). (Only an

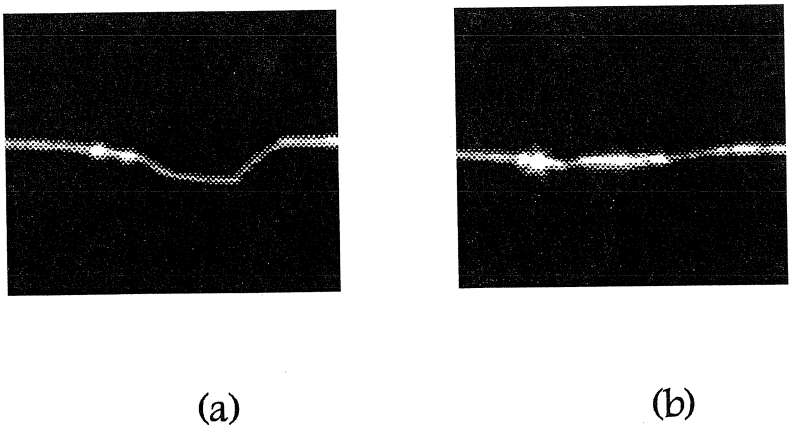

Fig. 5 Structured-light stripe images. (*a*) laser stripe for the seam tracking. (*b*) laser stripe on the sag. This figure illustrates the difference between the seam tracking and sag sensing in geometry. To emphasize the geometrical aspect, the submerged arc welding is used to decouple the arc light. In the seam tracking, the laser stripe is projected onto the groove ahead of the torch (*a*). It can be seen that the geometrical feature of the seam is apparent. If the square groove or fillet joints are encountered, the seam can be identified from the laser stripe even more easily. However, the geometry of sag could be complicated. The sag shown in (*b*) is acquired after the groove in (*a*) is welded. The border of sag is much more difficult to identify.

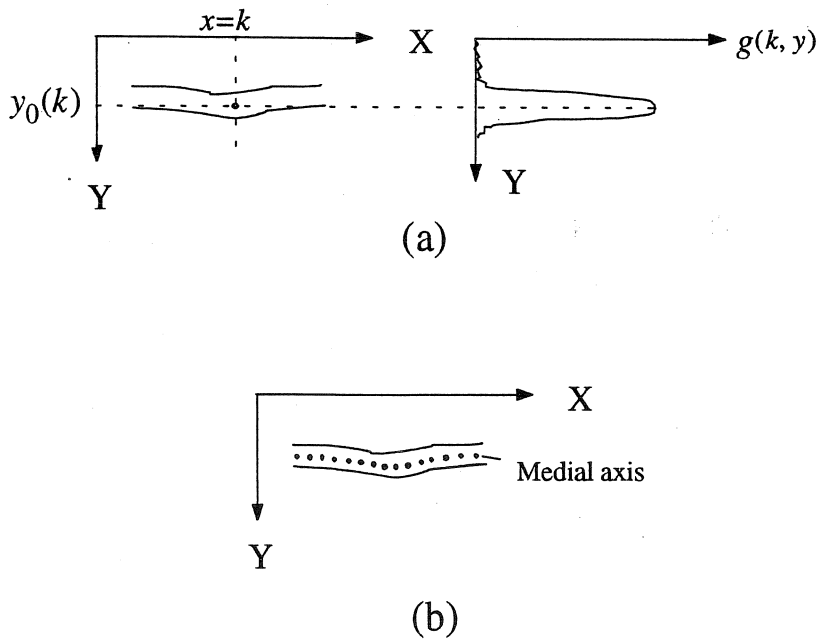

Fig. 6 Medial axis definition. (*a*) medial axis point. (*b*) medial axis. The grayness along the line $x = k$, denoted as $g(k, y)$, varies with the Y coordinate (*a*). Assume $g(k, y_0(k)) = \max_y g(k, y)$. $(k, y_0(k))$ is defined as the medial point along the line $x = k$. The medial axis is the set of such points for different X coordinates (*b*).

initial search of the full range is needed to detect $y_0(1)$ in Fig. 7.) The computational time is significantly reduced.

During actual welding, the continuity of the laser stripe can not be guaranteed (Fig. 8). In this case, the DTP may not work properly (Fig. 8). In order to overcome the influence of the discontinuity on the thinning, a modified dynamic thinning algorithm, the adaptive dynamic thinning algorithm (ADTA), is proposed. The ADTA first determines whether or not $(k, y_0(k))$ is on the laser stripe. If $y_0(k)$ is regarded to be on the laser stripe, $(k, y_0(k))$ is accepted as a medial point. Otherwise, the search for the medial point is extended to the full range along the Y direction. To determine whether or not $(k, y_0(k))$ is on the laser stripe, a grayness threshold for the laser stripe is required. It is known that the grayness of the laser stripe may not be uniform along the X direction. Thus, the grayness threshold must vary with the grayness of the laser stripe and an adaptive threshold is therefore needed. In this study, the following recursive equation has been used to calculate an adaptive threshold $T(k)$:

$$5T(k) = 5T(k-1) - g(y_0(k-6)) + g(y_0(k-1)) \quad (k = 1, 2, \ldots) \quad (2)$$

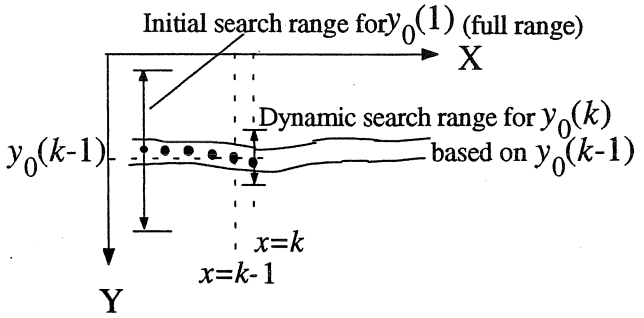

Fig. 7 Dynamic thinning of laser stripe. For the first medial point, the full range is searched. The succeeding medial points can be searched based on the Y coordinates of the previous medial points in a much smaller range. The figure shows that $y_0(k)$ is searched in a small neighborhood of $y_0(k-1)$.

where $g(y_0(j))$ is the grayness at point $(j, y_0(j))$. Since the grayness of the laser stripe is close to the maximum image grayness $2^8 - 1 = 255$, the recursive initials can be selected as:

$$\begin{cases} g(y_0(k)) = 200, & k \le 0 \\ T(0) = 200 \end{cases}$$

It can be seen that the threshold $T(k)$ has been calculated as an average grayness of the laser stripe (medial points) in the interval $[x = k - 5, x = k - 1]$. If

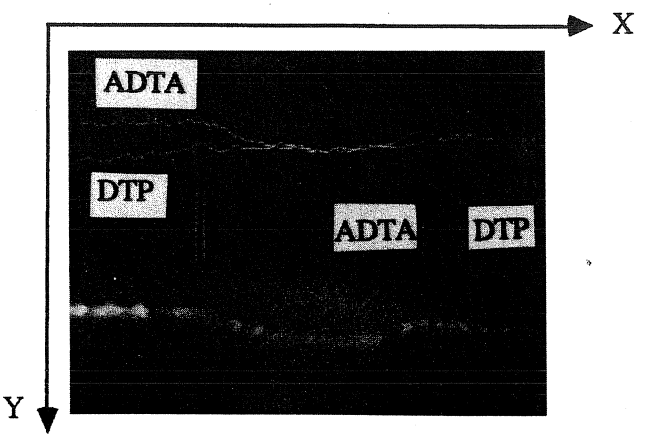

Fig. 8 Laser discontinuity. To reduce the influence of the laser stripe discontinuity, the initial medial point is searched at the middle along the X direction. Then the dynamic search is performed towards the X and negative X directions, respectively. However, because the laser stripe is not continuous in this image, the resultant medial axis extracted using the DTP has still been shifted from the laser stripe. When the adaptive algorithm ADTA is used, the discontinuity of laser stripe can be recognized and the laser stripe is re-located in the full range along the Y direction. The shift from the laser stripe can therefore be eliminated. Thus, the accurate medial axis is acquired by the ADTA.

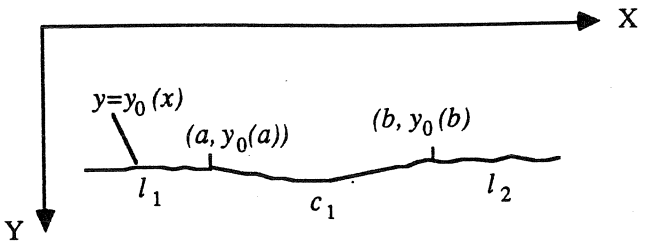

Fig. 9 Feature points of the medial axis. The feature points $(a, y_0(a))$ and $(b, y_0(b))$ are defined by the sag border.

$$T(k)K_T \le g(y_0(k)) \quad (1 > K_T > 0), \tag{3}$$

$(k, y_0(k))$ will be regarded to be bright enough and therefore will be accepted as a medial point. Otherwise, a search in the full range must be done. Extensive experiments have shown that $K_T = 0.8$ can yield acceptable performance. In this case, the adaptive dynamic thinning technique is robust to the various disturbances encountered during actual welding (Fig. 8). Also, the corresponding processing time is less than 80 ms on our 80386 + 80387 based experimental set-up.

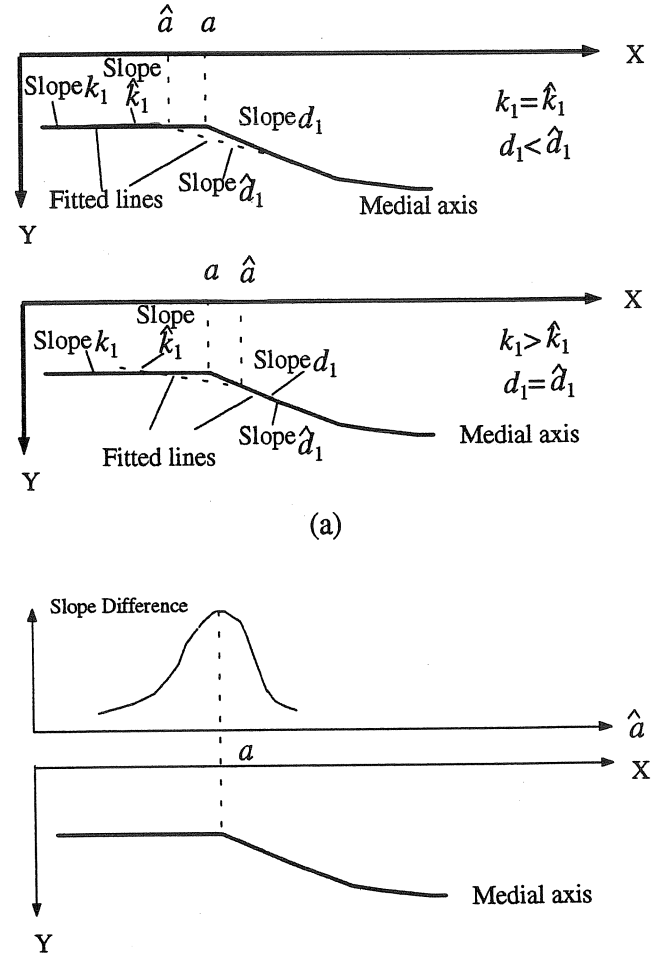

Fig. 10 Influence of the selected feature point on the slope difference. (*a*) When $\hat{a}$ is less than a, the slope of the fitted left line is accurate whereas the slope of the fitted right line is smaller than the actual value. When $\hat{a}$ is larger than a, the slope of the fitted right line is accurate whereas the slope of the fitted left line is larger than the actual value. (*b*) The slope difference varies with the selected feature point. Before the selected feature point reaches the actual feature point, the slope difference increases. After the selected feature point reaches the actual feature point, the slope difference decreases.

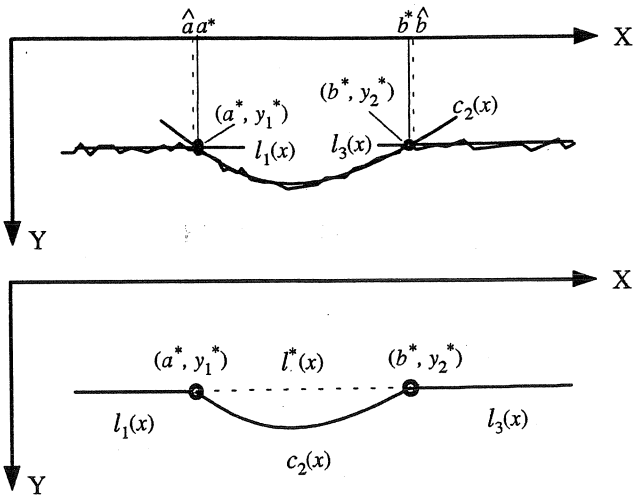

Fig. 11 Geometrical illustration for sag parameter calculation. The sag border is calculated using the fitted lines and curve. The line $l^*(x)$ is used as an estimate of the flat surface. The actual sag is described by the fitted $c_2(x)$. The area between the line $l^*(x)$ and curve $c_2(x)$ is the depression area.

6 Sag Range

The medial axis curve consists of three parts: two straight lines and a curve. The curve corresponds to the sag, and the two straight lines correspond to the unmolten part of the workpiece. These three parts are divided by two points, called the feature points of the medial axis. The feature points define the sag range. In order to compute the sag geometry parameters accurately, the feature points must be recognized unbiasedly. However, due to the disturbances from the arc light and the radiation from the weld pool, it is difficult to obtain an ideal medial axis of the laser stripe. Also, in many cases, the feature points may not be apparent since the sag depression is small. Thus, efforts must be made to obtain an unbiased estimate of feature points using statistical methods.

Due to the lack of success in using several conventional methods, an unbiased recognition algorithm is proposed based on a novel statistical feature point recognition principle, called the maximum principle of slope difference. The concept behind this algorithm is discussed below.

Assume a medial axis as shown in Fig. 9. Our intention is to determine the X coordinates of the feature points $(a, y_0(a))$ and $(b, y_0(b))$, (i.e., a and b). In the following discussion, only a is considered since b can similarly be recognized.

Suppose the equation of the straight line on the left-hand side of a is:

$$y_0 = k_0 + k_1 x + \epsilon_x, \quad x \le a \tag{4}$$

The curve on the right-hand side of a in a vicinity of a can be approximated by a linear equation:

$$y_0 = d_0 + d_1 x + \epsilon_x, \quad x > a \tag{5}$$

where $\epsilon_x - N(0, \sigma^2)$ is the Gaussian white noise representing the error of the medial axis extraction.

Suppose $\hat{a}$ is the X coordinate of a point on the medial axis on the left-hand side of a ($\hat{a} \le a$). We estimate (k_0, k_1) and (d_0, d_1) by the least squares method based on the point set $(\hat{a} - j, y_0(\hat{a} - j))$ $(j = 1, 2, \ldots, M)$ and $(\hat{a} + j, y_0(\hat{a} + j))$ $(j = 1, 2, \ldots, M)$, respectively. Hence, it can be shown that

$$(\hat{k}_0, \hat{k}_1)^T = (\Phi_1^T\Phi_1)^{-1}\Phi_1^T(\Phi_1(k_0, k_1)^T + \epsilon_1)$$
$$= (k_0, k_1)^T + (\Phi_1^T\Phi_1)^{-1}\Phi_1^T\epsilon_1$$

where ϵ_1 is a Gaussian white noise vector and Φ_1 is:

$$\Phi_1 = \begin{pmatrix} 1 & 1 & \cdots & 1 \\ \hat{a} - M & \hat{a} - (M-1) & \cdots & \hat{a} - 1 \end{pmatrix}^T$$

Also, we can obtain:

$$(\hat{d}_0, \hat{d}_1)^T = (\Phi_2^T\Phi_2)^{-1}\Phi_2 Y_2$$

where

$$\Phi_2 = \begin{pmatrix} 1 & 1 & \cdots & 1 \\ \hat{a} + 1 & \hat{a} + 2 & \cdots & \hat{a} + M \end{pmatrix}^T = \begin{pmatrix} A_1 \\ A_2 \end{pmatrix} \quad (6)$$

$$Y_2 = A_1K + A_2D + \epsilon_2 = \Phi_2 D - (A_1D - A_1K) + \epsilon_2$$
$$= \Phi_2 D - \Delta Y_0 + \epsilon_2$$

where ϵ_2 is the Gaussian white noise vector as well, and

$$A_1 = \begin{pmatrix} 1 & \cdots & 1 & 0_{2\times(\hat{a}+M-a+1)} \\ \hat{a} + 1 & \cdots & a - 1 & \end{pmatrix}^T$$

$$A_2 = \begin{pmatrix} 0_{2\times(a-\hat{a}-1)} & 1 & \cdots & 1 \\ & a & \cdots & \hat{a} + M \end{pmatrix}^T$$

$$D = (d_0, d_1)^T$$
$$K = (k_0, k_1)^T$$

$$\begin{cases} \Delta Y_0 = (\Delta y_0(\hat{a} + 1), \ldots, \Delta y_0(a - 1) \quad : \quad 0_{2\times(\hat{a}+M-a+1)})^T = A_1D - A_1K \\ \Delta y_0(j) = d_0 + d_1 j - k_0 - d_1 j \qquad\qquad \hat{a} + 1 \le j \le a - 1 \end{cases} \quad (7)$$

Thus,

$$(\hat{d}_0, \hat{d}_1)^T = (d_0, d_1)^T(\Phi_2^T\Phi_2)^{-1}\Phi_2^T\Delta Y_0 + (\Phi_2^T\Phi_2)^{-1}\Phi_2^T\epsilon_2$$

The expectation of $\hat{d}_1 - \hat{k}_1$ is given by

$$E(\hat{d}_1 - \hat{k}_1) = d_1 - k_1 - \{(\Phi_2^T\Phi_2)^{-1}\}_2\Phi_2^T\Delta Y_0 \quad (8)$$

where $\{(\Phi_2^T\Phi_2)^{-1}\}_2$ represents the second row of the matrix $(\Phi_2^T\Phi_2)^{-1}$, and

$$\Phi_2^T\Delta Y_0 = \left(\sum_{x=\hat{a}+1}^{a-1} \Delta y_0(x(k)), \sum_{x=\hat{a}+1}^{a-1} x\Delta y_0(x(k))\right)^T$$

Similarly, in the case of $\hat{a} \ge a$, we can obtain the expectation of $E(\hat{d}_1 - \hat{k}_1)$ as well.

Denote

$$\nu(\hat{a}) = E(\hat{d}_1(\hat{a}) - \hat{k}_1(\hat{a})) \quad (9)$$

It can be shown that

$$\nu(a) = \max_{\hat{a}\in(a-M,a+M)} \nu(\hat{a}) \quad (10)$$

That is, $\nu(\hat{a})$ reaches its maximum at $\hat{a} = a$. This is referred to as the Maximum Principle of Slope Difference in this study (Appendix). In fact, if $\hat{a} < a$, k_1 will be accurately estimated. However, the estimated d_1 tends to decrease as $\hat{a}$ decreases. If If $\hat{a} > a$, k_1 will tend to increase whereas d_1 will be accurately estimated (Fig. 10(a)). Thus, the estimated slope difference $\hat{d}_1 - \hat{k}_1$ tends to reach its maximum at $\hat{a} = a$ (Fig. 10(b)). Consequently, $\hat{a}$ selected using the following criterion is an unbiased estimate of a:

$$\hat{a}: \max_{\hat{a}\in(a-M,a+M)} (\hat{d}_1(\hat{a}) - \hat{k}_1(\hat{a})) \quad (11)$$

That is, the mathematical expectation of the estimated $\hat{a}$ is equal to a. Similarly, the unbiased estimate of b can be acquired.

In order to reduce the on-line computational burden, the second rows in both $(\Phi_1^T\Phi_1)^{-1}$ and $(\Phi_2^T\Phi_2)^{-1}$ are calculated off-line prior to the welding. Thus, only 9 on-line float operations are needed for the slope difference computation. Suppose that 20 slope difference computations are required in searching for the two feature points. Then the total number of float operations for feature points recognition is 180. (The size of the point set M is selected to be 30 by experiments.) For our experimental set-up, these computations will require about 12 ms.

7 Geometrical Parameters

In order to calculate the sag geometric parameters, the left, middle, and right portions of the medial axis are fitted to a linear, a quadratic, and a linear model, respectively, utilizing the least squares method. Suppose the resultant models are $l_1(x)$

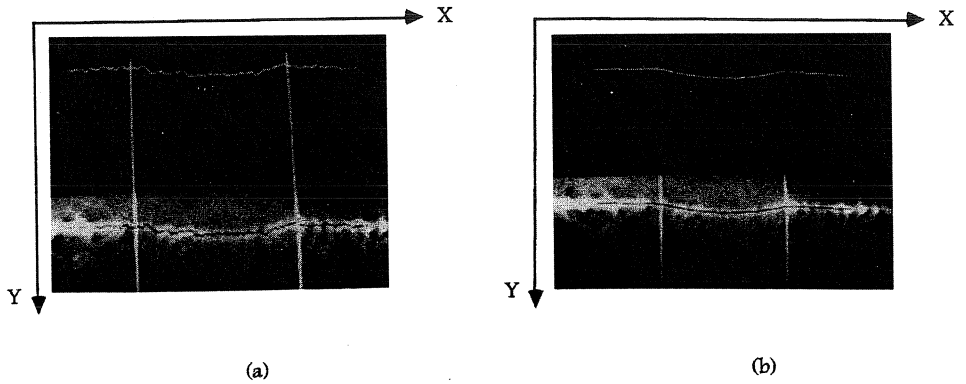

(a) (b)

Fig. 12 Processing of the typical sag-stripe image. (*a*) medial axis and feature points. The laser stripe and its medial axis are displayed on the bottom. The medial axis is shown above. Two vertical lines show the recognized positions of the feature points. (*b*) modeled medial axis. The medial axis can be smoothed through fitting three curves. The smoothed curves are recognized to represent the actual weld cross shape.

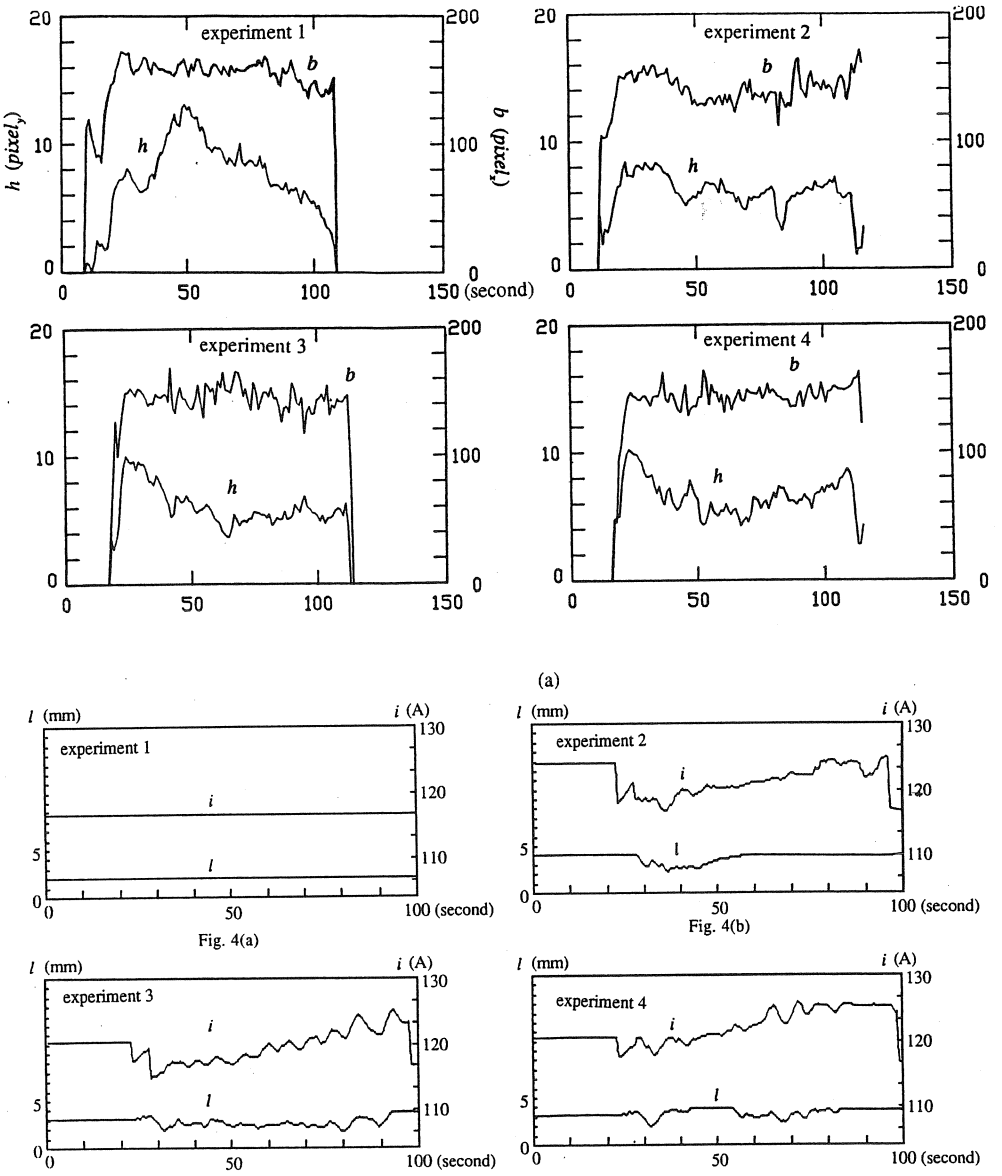

Fig. 13 On-line measurements of sag geometry. (*a*) measured sag parameters. (*b*) welding parameters. Four experiments were performed using the current and arc length shown in (*b*). For experiment 1, a heat sink was applied in the middle portion of the weld by changing the plate width. The measurements in (*a*) were acquired during welding by the developed image system. The measurement accuracy was confirmed by displaying the image processing results on the original image as shown in Fig. 12(*b*). The units for *b* and *h* are pixel$_x$ = 0.05 mm and pixel$_y$ = 0.0436 mm, respectively.

$(x \le a)$, $c_2(x, x^2)$ $(a < x < b)$ and $l_3(x)$ $(x \ge b)$, respectively (Fig. 11). The point of intersection of l_1 and c_2 is (a^*, y_1^*), the point of intersection of c_2 and l_3 is (b^*, y_2^*). Denote the straight line connecting (a^*, y_1^*) and (b^*, y_2^*) as l^*. Then, we can employ the following equations to compute the sag geometric parameters of interest (Fig. 11):

$$\text{Weld width:} \quad b^* - a^*$$

$$\text{Average Depression Depth:} \quad \frac{\int_{a^*}^{b^*} (c_2 - l^*)dx}{(b^* - a^*)}$$

It can be seen that the proposed image processing technique depends on two novel algorithms: the adaptive dynamic thinning algorithm for extraction of the medial axis of the laser stripe and the unbiased algorithm for recognition of feature points of the medial axis. These solved the conflict between computational burden and the algorithm properties. In order to verify the algorithm performance, the extracted feature points and fitted medial axis have been displayed and compared with the original images on the monitor during welding. It was shown that the algorithm can function well during actual welding when various noises are present. Figure 12 illustrates the extracted medial axis, feature points and smoothed medial axis (l_1, c_2 and l_3) for the typical image shown in Fig. 4. The algorithm was programmed in $C++$. The total time for the image sampling, image processing and sag parameter computation is less than 200 ms on our 80387 + 80386 based experimental set-up. Both the algorithm performance and speed are satisfactory. Thus, this sensing technique has been incorporated to develop a closed-loop control system [14].

8 Application Experiments

On-line Sag Measurements. The developed sensing technique has been applied to measure the sag during welding. The

measurements from four experiments are plotted in Fig. 13(a) where l and i are the arc length and welding current, respectively. The used arc length and current are illustrated in Fig. 13(b). The variations in the arc length and welding current are used to generate varied sag parameters. Stainless steel 304 is used. The thickness of the plates is 3 mm. The dimensions of the workpiece are 250 mm in length and 150 mm in width. Butt welds are made using DC GTA welding with argon shielding. The torch speed is 2 mm/s.

The measurements in Fig. 13(a) were acquired during welding. In order to show the location of the measured sag relative to the workpiece, the time was measured using the period needed for the torch to travel from the workpiece edge, instead of the actual welding time. The sampling interval along the seam was 1 mm. It was observed that the extracted medial axis and feature points were accurate. Thus, the sag parameters can be calculated with sufficient accuracy.

Applications in Feedback Control. A feedback controller has been developed to control the sag geometry using the measured feedback. Both h and b are adjusted using the current and arc length in order to achieve the desired full penetration status and uniform weld appearance, respectively. It is known that the feedback of the controlled parameters plays a critical role in acquiring a closed-loop control. If accurate feedback measurements can be acquired, a closed-loop control system will be achieved by selecting a proper control algorithm. Based on the characteristics of full penetration welding, the generalized predictive control proposed by Clarke et al. [18] has been selected to control the sag parameters [14]. This algorithm has been used to control the area of the weld pool in a previous study [19].

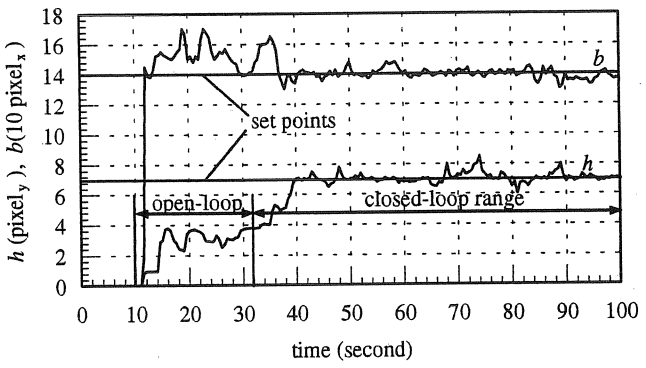

(a)

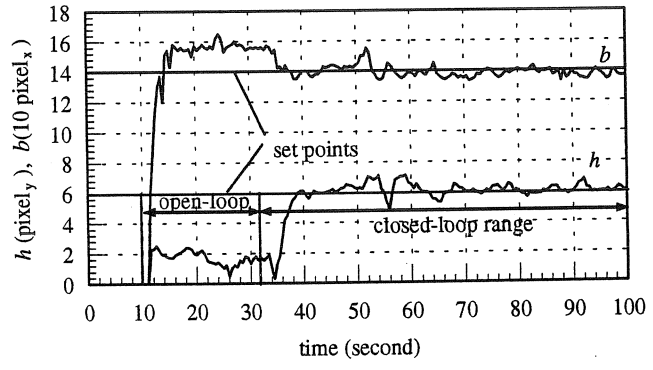

(b)

Fig. 14 Feedback measurements in closed-loop controls. (*a*) control experiment 1. (*b*) control experiment 2. In the open-loop range, large errors are observed between the actual sag geometrical parameters and their set-points. By providing the controller with the feedback of the sag parameters, the welding parameters have been changed to reach the desired levels of the sag parameters.

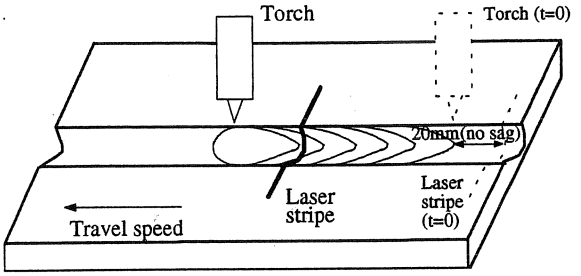

Fig. 15 Sag range and initial electrode and laser locations. The range defined by the initial positions of the laser stripe and electrode has no sag.

Figure 14 shows measured feedback parameters during two closed-loop control experiments. Large initial errors between the set-points and actual values of the sag parameters can be observed in the open-loop range. It is known that the laser stripe is 20 mm behind the electrode. Also, the sag will only be present ahead of the initial location of the electrode (Fig. 15). Thus, there is a 10 second period during which no sag parameters can be acquired. During this period, the welding parameters can only be selected based on the *a priori* knowledge. An open-loop control is actually applied. After this period, the measured feedback will be acquired. By knowing the difference between the actual sag parameters and their set-points, the welding parameters (current and arc length) are then changed to acquire the desired sag parameters. It can be observed in Fig. 14 that the actual sag parameters have approached their set-points after the feedback is provided.

9 Conclusions

In order to reduce the feedback delay, the laser stripe must be projected near the pool rear. In this case, strong disturbances from the hot metal corrupt the image, even though a suitable narrow-band optical filter has been incorporated. Also, the sag border is often inapparent because of the small weld depression.

A real-time image processing technique has been proposed to acquire accurate sag geometric parameters. This technique depends on two novel image processing algorithms: an adaptive dynamic algorithm which extracts the medial axis of the laser stripe and an unbiased algorithm which recognizes the feature points of the medial axis. The effectiveness of the developed sensing system and real-time processing technique has been verified for accuracy and processing speed through extensive experimentation. The proposed sensing technique provides an effective feedback to control the sag geometry. Because of the correlation between the sag geometry and back-side bead width, the full penetration status can therefore be controlled in the root pass.

References

1 Zhang, Y. M., et al., 1993, "Determining Joint Penetration in GTAW with Vision Sensing of Weld Face Geometry," *Welding Journal,* Vol. 72, No. 10, pp. 463s–469s.

2 Xiao, Y. H., and Ouden, G. den, 1993, "Weld Pool Oscillation during GTA Welding of Mild Steel," *Welding Journal,* Vol. 72, No. 8, pp. 428s–434s.

3 Xiao, Y. H., and Ouden, G. den, 1990, "A Study of GTA Weld Pool Oscillation," *Welding Journal,* Vol. 69, No. 8, pp. 298s–293s.

4 Yang, J., et al., 1994, "Ultrasonic Weld Penetration Depth Sensing with a Laser Phased Array," *Proceedings of 1994 ASME International Mechanical Engineering Congress,* PED-Vol. 68-1, Manufacturing Science and Technology, pp. 245–254, Nov. 6–11, Chicago, IL.

5 Rokhlin, S. I., and Guu, A. C., 1993, "A Study of Arc Force, Pool Depression, and Weld Penetration during Gas Tungsten Arc Welding," *Welding Journal,* Vol. 72, No. 8, pp. 381s–390s.

6 Lin, M. L., and Eagar, T. M., 1985, "Influence of Arc Pressure on Weld Pool Geometry," *Welding Journal,* Vol. 64, No. 6, pp. 163–169s; "Sensing of Weld Face Geometry," *Welding Journal,* Vol. 64, No. 6, pp. 163s–169s.

7 Kanatani, K. I., 1984, "Detection of Surface Orientation and Motion from Texture by a Stereological Technique," *Artificial Intelligence,* Vol. 23, pp. 213–237.
8 Lee, C. H., and Rosenfeld, A., 1985, "Improved Methods of Estimating Shape from Shading Using the Light Source Coordinate System," *Artificial Intelligence,* Vol. 26, pp. 125–143.
9 Luh, J. Y. S., and Klaasen, J. A., 1985, "A Three-Dimensional Vision by Off-Shelf System with Multi-Cameras," *IEEE Transactions on Pattern Analysis and Intelligence,* PAMI-7(1), pp. 35–45.
10 Nayak, N., et al. 1987, "Adaptive Real-Time Intelligent Seam Tracking System," *Journal of Manufacturing Systems,* Vol. 6, No. 3, pp. 241–245.
11 Andrew, N., et al. 1989, "An Adaptive Seam Tracker for Welding Heavy-Section Aluminum," *IEEE Transactions on Industrial Application,* Vol. 25, pp. 658–663.
12 Blais, F. Rioux, M., and Beraldin, J.-A., 1988, "Practical Considerations for a Design of a High Precision 3-D Laser Scanner System," *SPIE,* Vol. 959, Optomechanical and Electro-Optical Design of Industrial Systems, pp. 225–246.
13 Cielo, P., and Dufour, M., 1988, "Optical Inspection in Hostile Industrial Environments: Single-Sensor vs. Imaging Methods," *SPIE,* Vol. 959 Optomechanical and Electro-Optical Design of Industrial Systems, pp. 87–115.
14 Zhang, Y. M., Kovacevic, R., and Wu, L., 1996, "Dynamic Analysis and Identification of Gas Tungsten Arc Welding Process for Weld Penetration Control," ASME JOURNAL OF ENGINEERING FOR INDUSTRY, Vol. 118, No. 1, pp. 123–136.
15 Pietrzak, K. A., 1989, "Robust Seam Tracking Algorithm Based on Majority Volting Logic," *Proc. SPIE,* Vol. 1197, pp. 218–229.
16 Hirai, A., et al., 1988, "Welding Robot with Visual Seam Tracking Sensor," *Proc. USA-Japan Symposium on Flexible Automation—Crossing Bridges: Advances in Automation and Robots,* ASME, New York, NY, USA, pp. 1055–1060.
17 Davies, E. R., and Plummer, A. P. N., 1981, "Thinning Algorithms: A Critique and a New Methodology," *Pattern Recognition,* Vol. 14, pp. 53–63.
18 Clarke, D. W., Mohtadi, C., and Tuffs, P. S., 1987, "Generalized Predictive Control—Part I. The Basic Algorithm," *Automatica,* Vol. 23, No. 2, pp. 137–148.
19 Kovacevic, R., Zhang, Y. M., and Ruan, S., 1995, "Sensing and Control of Weld Pool Geometry for Automated GTA Welding," ASME JOURNAL OF ENGINEERING FOR INDUSTRY, Vol. 117, No. 2, pp. 210–222.

APPENDIX

The Maximum Principle of Slope Difference

Theorem: Suppose there are two continuous random straight lines:

$$\begin{cases} y_0 = k_0 + k_1 x + \epsilon_x & x \le a \\ y_0 = d_0 + d_1 x + \epsilon_x & x > a \end{cases}$$

and

$$k_0 + k_1 a = d_0 + d_1 a$$

where $\epsilon_x - N(0, \sigma^2)$, $\hat{k}_1(\hat{a})$ is the least squares estimate of k_1 obtained based upon $y_0(\hat{a} - j)$ $(j = 1, \ldots, M)$, and $\hat{d}_1(\hat{a})$ is the least squares estimate of d_1 obtained based upon $y_0(\hat{a} + j)$ $(j = 1, \ldots, M)$. Then the mathematical expectation $E(\hat{d}_1(\hat{a}) - \hat{k}_1(\hat{a}))$ approaches its unique maximum value at $\hat{a} = a$ in the interval $\hat{a} \in (a - M, a + M)$ and

$$E(\hat{d}_1(a) - \hat{k}_1(a)) = \max_{\hat{a} \in (a-M, a+M)} E(\hat{d}_1(\hat{a}) - \hat{k}_1(\hat{a})) = d_1 - k_1$$

Proof: If we can prove the following are true, our theorem will be true:

$$E(\hat{d}_1(\hat{a}) - \hat{k}_1(\hat{a})) > E(\hat{d}_1(\hat{a} - 1) - \hat{k}_1(\hat{a} - 1)) \qquad a - M < \hat{a} \le a \quad \text{(a1)}$$

$$E(\hat{d}_1(a) - \hat{k}_1(a)) = d_1 - k_1 \quad \text{(a2)}$$

$$E(\hat{d}_1(\hat{a}) - \hat{k}_1(\hat{a})) > E(\hat{d}_1(\hat{a} + 1) - \hat{k}_1(\hat{a} + 1)) \qquad a \le \hat{a} < a + M \quad \text{(a3)}$$

Since the proofs of (a1) and (a3) are symmetrical problems, only (a1) and (a2) need to be proven.

From (8) it can be seen that when $\hat{a} \le a$,

$$E(\hat{d}_1(\hat{a}) - \hat{k}_1(\hat{a})) = d_1 - k_1 - \{(\Phi_2^T \Phi_2)^{-1}\}_2 \Phi_2^T \Delta Y_0 \quad \text{(a4)}$$

From (6) we can obtain:

$$\Phi_2^T \Phi_2 = \begin{pmatrix} M & \sum_{j=1}^{M} (\hat{a} + j) \\ \sum_{j=1}^{M} (\hat{a} + j) & \sum_{j=1}^{M} (\hat{a} + j)^2 \end{pmatrix}$$

Thus,

$$(\Phi_2^T \Phi_2)^{-1} = \begin{pmatrix} \sum_{j=1}^{M} (\hat{a} + j)^2 & -\sum_{j=1}^{M} (\hat{a} + j) \\ -\sum_{j=1}^{M} (\hat{a} + j) & M \end{pmatrix} \frac{1}{f(M)}$$

$$= \begin{pmatrix} \sum_{j=1}^{M} (\hat{a} + j)^2 & -\sum_{j=1}^{M} (\hat{a} + j) \\ -M\left(\hat{a} + \frac{1+M}{2}\right) & M \end{pmatrix} \frac{1}{f(M)}$$

where

$$f(M) = M[M(\hat{a}^2 + \hat{a}(1 + M)) + \sum_{j=1}^{M} j^2] - M^2\left(\hat{a} + \frac{1+M}{2}\right)^2$$

Thus,

$$\{(\Phi_2 \Phi_2)^{-1}\}_2 = \frac{M}{f(M)} \left(-\left(\hat{a} + \frac{1+M}{2}\right), 1\right)$$

Let

$$\delta(\hat{a}) = \left(-\left(\hat{a} + \frac{1+M}{2}\right), 1\right)$$

$$\sigma(\hat{a}) = \Phi_2^T \Delta Y_0 = \left(\sum_{x=\hat{a}+1}^{a-1} \Delta y_0(x), \sum_{x=\hat{a}+1}^{a-1} x \Delta y_0(x)\right)^T$$

$$F(M) = M / f(M)$$

where $\Delta y(x) = d_0 + d_1 x - k_0 - k_1 x$ (see (7)). Then

$$\begin{aligned} &\hat{E}(\hat{d}_1(\hat{a} + 1) - \hat{k}_1(\hat{a} + 1)) \\ &= d_1 - k_1 - F(M)\delta(\hat{a} + 1)\sigma(\hat{a} + 1) \\ &= d_1 - k_1 - F(M)\{\delta(\hat{a}) - (1, 0)\} \\ &\quad \times \{\sigma(\hat{a}) - (1, \hat{a} + 1)^T \Delta y_0(\hat{a} + 1)\} \\ &= d_1 - k_1 - F(M)\{\delta(\hat{a})\sigma(\hat{a}) - \sum_{x=\hat{a}+1}^{a-1} \Delta y_0(x) \\ &\quad - (-\hat{a} - (1 + M)/2 + \hat{a} + 1) \\ &\quad \times \Delta y_0(\hat{a} + 1) + \Delta y_0(\hat{a} + 1)\} \\ &= d_1 - k_1 - F(M)\left\{\delta(\hat{a})\sigma(\hat{a}) \right. \\ &\quad \left. - \sum_{x=\hat{a}+1}^{a-1} \Delta y_0(x) + \frac{1+M}{2} \Delta y_0(\hat{a} + 1)\right\} \\ &= E(\hat{d}_1(\hat{a}) - \hat{k}_1(\hat{a})) + F(M)\left\{\sum_{x=\hat{a}+1}^{a-1} \Delta y_0(x) \right. \\ &\quad \left. - \frac{1+M}{2} \Delta y_0(\hat{a} + 1)\right\} \quad \text{(a5)} \end{aligned}$$

Since Δy_0 is linear (see (7)), and since $\Delta y_0(a) = 0$, the following can be produced based on the equation of the triangular area:

$$\sum_{x=\hat{a}+1}^{a-1} \Delta y_0(x) = \tfrac{1}{2}(a - 1 - \hat{a} - 1 + 1)\Delta y_0(\hat{a} + 1)$$

$$= \tfrac{1}{2}(a - \hat{a} - 1)\Delta y_0(\hat{a} + 1).$$

Thus,

$$\left\{ \sum_{x=\hat{a}+1}^{a-1} \Delta y_0(x) - \frac{1 + M}{2} \Delta y_0(\hat{a} + 1) \right\}$$

$$= \tfrac{1}{2}\{(a - \hat{a}) - (M + 2)\}\Delta y_0(\hat{a} + 1)$$

Since

$$\Delta y_0(\hat{a} + 1) > 0, \quad a - M < \hat{a} + 1 < a$$

$$\Delta y_0(a) = 0$$

$$(a - \hat{a}) - (M + 2) < 0, \quad a - M < \hat{a} + 1 < a,$$

we can acquire:

$$\sum_{x=\hat{a}+1}^{a-1} \Delta y(x) - \frac{1}{1 + M} \Delta y_0(\hat{a} + 1)$$

$$\begin{cases} <0 & a - M < \hat{a} + 1 < a \\ =0 & \hat{a} + 1 = a \end{cases} \tag{a6}$$

On the other hand,

$$f(M)/M = M\hat{a}^2 + M\hat{a}(1 + M)$$

$$- M(1 + M)^2/4 - M\hat{a}^2 - \hat{a}M - M^2\hat{a}$$

$$+ \sum_{j=1}^{M} j^2 = \frac{4 \sum_{j=1}^{M} j^2 - M(M + 1)^2}{4} = \frac{M(M^2 - 1)}{12}$$

Thus,

$$F(M) = M/f(M) > 0 \quad M > 1 \tag{a7}$$

Therefore, from (a7), (a6) and (a5) we can immediately obtain:

$$E(\hat{d}_1(\hat{a} + 1)) - \hat{k}_1(\hat{a} + 1) > E(\hat{d}_1(\hat{a}) - \hat{k}_1(\hat{a})) \quad \hat{a} + 1 < a$$

From (a4) and the definition of ΔY_0, we can obtain:

$$E(\hat{d}_1(a) - \hat{k}_1(a)) = d_1 - k_1$$